Prepublished copy

Nature Environment & Pollution Technology

This is a peer-reviewed prepublished version of the paper to be published in Vol. 25, No. 3, September 2026 issue

Type of the Paper (Original Research Paper)

An Assessment of Biopolymer-Based Metal Oxide Nanoparticles for the Removal of Heavy Metals from Water

Koffi Sossou[1]†, Alfred O. Mayabi[2], Zeraebruk Negusse Kahsay [2] and Charles K. Cheruiyot [2]

[1]Department of Civil Engineering, Pan African University Institute for Basic Sciences, Technology and Innovation (PAUSTI-JKUAT), Kenya

[2] Department of Civil, Construction and Environmental Engineering, Jomo Kenyatta University of Agriculture and Technology, Nairobi, Kenya

†Corresponding author: Koffi Sossou: sossou.koffi@students.jkuat.ac.ke

ORCID ID of Author 1†: https://orcid.org/0009-0001-9417-7020

Key Words	Adsorption; Banana peels; Kinetic study, Chemisorption; Metal oxide nanoparticles; Removal of heavy metals
DOI	https://doi.org/10.46488/NEPT.2026.v25i03.D1891 (DOI will be active only after the final publication of the paper)
Citation for the Paper	Sossou, K., Mayabi, A.O., Kahsay, Z.N. and Cheruiyot, C.K., 2026. An assessment of biopolymer-based metal oxide nanoparticles for the removal of heavy metals from water. *Nature Environment and Pollution Technology*, 25(3), D1891. https://doi.org/10.46488/NEPT.2026.v25i03.D1891

Abstract

Water contamination by toxic heavy metals remains a persistent environmental and public health challenge, demanding cost-effective and sustainable remediation approaches. In this study, a banana peel–based metal oxide nanocomposite (Fe_3O_4/TiO_2/BP) was synthesized via a combined co-precipitation and hydrothermal-assisted method and evaluated for the adsorption of Cr(VI), Cd(II), and Pb(II) from aqueous solutions. Characterization using FTIR, SEM–EDS, and XPS confirmed the successful incorporation of Fe_3O_4 and TiO_2 nanoparticles into the banana peel matrix, resulting in enhanced surface functionality and magnetic separability. The equilibrium data were best described by the Langmuir and Redlich–Peterson isotherm models, indicating monolayer adsorption with maximum capacities of 14.4 mg/g for Cr(VI), 10.9 mg/g for Cd(II), and 100 mg/g for Pb(II). Kinetic modeling revealed that adsorption followed the pseudo-second-order model ($R^2 = 0.97$–0.93). The Fe_3O4/TiO_2/BP nanocomposite exhibited excellent performance and competitive adsorption capacity compared to other reported metal oxide-based adsorbents, confirming its potential as a sustainable, low-cost material for multicomponent heavy metal removal and agricultural waste valorization.

1-INTRODUCTION

Environmental pollution caused by inadequate wastewater management has drawn significant global attention in recent decades, particularly due to the release of toxic heavy metals into aquatic environments. Wastewater containing heavy metals, dyes, and organic pollutants poses severe risks to ecosystems and human health, as these contaminants are non-biodegradable, persistent, and capable of bioaccumulation (Sossou et al. 2024, A. Mishra et al. 2022). In countries with limited treatment infrastructure and weak regulatory enforcement, heavy metal contamination of water resources is further exacerbated (Smyth et al. 2024; Strategies et al. 2024).

Conventional wastewater treatment methods, including chemical precipitation, ion exchange, and membrane filtration, often suffer from high operational costs, secondary sludge generation, and low selectivity toward multiple coexisting contaminants (Razzak et al. 2022). As a result, adsorption using low-cost and environmentally friendly materials has emerged as a promising alternative for heavy metal removal. In this context, biosorbents derived from agricultural residues have gained increasing attention due to their abundance, biodegradability, and alignment with circular economy principles.

Banana peel is one such agricultural by-product that has been extensively investigated as a low-cost biosorbent. According to the Food and Agriculture Organization of the United Nations (FAO 2024), approximately 3.5 million tonnes of banana peel waste are generated globally each year. Much of this biomass is disposed of in open dumps or landfills, leading to environmental hazards such as leachate generation, greenhouse gas emissions during decomposition, and contamination of soil and water resources (Mor et al. 2023, Sial et al. 2019). Nevertheless, banana peel contains significant amounts of cellulose, hemicellulose, lignin, pectin, and starch, providing abundant functional groups such as hydroxyl and carboxyl moieties capable of interacting with metal ions (Pokharel et al. 2018; Liew et al. 2018; Mehmood et al. 2025; Mishra et al. 2023). Despite these advantages, raw banana peel or unmodified biopolymers often exhibit limited adsorption capacity and reduced effectiveness in multicomponent systems due to competitive adsorption among coexisting metal ions (Gupta et al. 2025).

To overcome these limitations, the integration of metal oxide nanoparticles with biomass-based adsorbents has been widely explored. Nanomaterials such as iron oxides and titanium dioxide offer high surface areas, enhanced surface reactivity, and improved physicochemical stability, leading to improved adsorption performance (Togun et al. 2025; Sossou et al. 2024). In particular, magnetite (Fe_3O_4) nanoparticles are attractive due to their strong affinity for metal ions and magnetic properties that facilitate easy separation from treated water, while TiO_2 contributes additional adsorption sites and chemical stability (Lellala et al. 2024). Despite these advances, most previous studies have focused on single-metal systems or non-magnetic banana peel modifications, limiting their applicability to real wastewater containing multiple competing contaminants. Therefore, this study aims to synthesize and evaluate a Fe_3O_4/TiO_2/banana peel nanocomposite for the removal of Cr(VI), Cd(II), and Pb(II) from aqueous solutions under multicomponent conditions. The results provide insight into the potential of this nanocomposite as a low-cost, sustainable, and environmentally friendly material for heavy metal remediation.

2. MATERIALS AND METHODS

2.1. Adsorbent's preparation and characterization

2.1.1. Hydrothermal-Assisted Nanocomposite Synthesis of Iron Oxide

Hydrothermal-assisted synthesis was employed to produce iron oxide-based nanocomposites. Naturally sourced low-grade iron oxides were obtained from Ollesos Company (Kenya) and used as raw materials without further chemical modification. 100 g of the mixed iron oxide powders were dispersed in 100 mL of distilled water and stirred using a magnetic stirrer (40 rpm/min) for 2 hours to achieve a uniform suspension. The pH of the mixture was adjusted to 7 using NaOH solution. The resulting suspension was transferred into a Teflon-lined stainless steel autoclave and subjected to hydrothermal treatment at 105 °C for 12 hours.

After natural cooling to room temperature, the solid product was collected by centrifugation, washed three times with ethanol, and then with distilled water to remove any residual impurities. The washed material was dried in a hot air oven at 80 °C and then calcined in a furnace at 500°C for 6 hours. The calcined powder was then ground using a mortar and pestle to obtain a fine, homogeneous nanocomposite powder (Fig. 1).

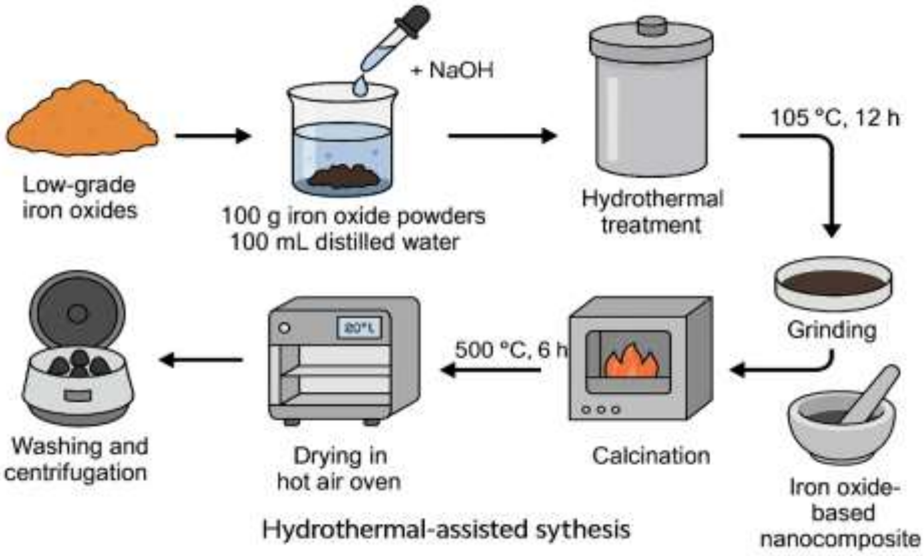

Fig. 1: Hydrothermal-assisted nanocomposite synthesis of iron oxide.

2.1.2. Hydrothermal synthesis of Titanium dioxide

TiO_2 nanoparticles were synthesized by a hydrothermal method with slight modifications to reported procedures (Keerthana et al. 2018; Zanganeh et al. 2011). Commercial TiO_2 powder (Degussa P25, Evonik; 99.9% purity, anatase/rutile ratio 90:10, ~10 nm) was used as the precursor. Typically, 1 g of TiO_2 was dispersed in 50 mL of 10 M NaOH solution under vigorous stirring for 40 min, then transferred to a 50 mL Teflon-lined stainless-steel autoclave and heated at 200 °C for 48 h.

The resulting precipitate was cooled to room temperature, washed repeatedly with deionized water (resistivity $\geq$15 MΩ·cm) and 0.1 M HCl until neutral pH was achieved, and then separated by centrifugation (5000 rpm, 10 min). The product was dried at 60 °C for 1 h and calcined at 250 °C for 2 h in air to enhance crystallinity and minimize residual sodium.

To evaluate the effect of the alkaline medium, the synthesis was repeated using KOH instead of NaOH. The obtained TiO_2 nanoparticles were stored in a desiccator until further characterization and application

2.1.3. Biopolymer materials

For the preparation of the biopolymer, banana peels were locally sourced from Juja Market (Kenya), washed three times with tap water, cut into small pieces (3-4 cm), cut peels air-dried for one week, and in a hot air oven at 105 °C for 12 hours. The dried peels were then crushed using a mortar and pestle to obtain a fine powder, which was sieved through a 200 µm mesh to ensure uniform particle size. The resulting powder was used as a raw material for the homogeneous nanocomposite. The morphology of banana peel powder was observed by scanning electron microscopy (SEM) micrographs of the peels and biochar surfaces.

2.2. Characterization of the materials

The iron oxide, titanium dioxide nanomaterial and biopolymer powder were characterized to comprehensively determine their physical, chemical, and structural properties. Parameters such as surface area, pore size distribution, chemical composition, elemental states, and magnetic behavior were evaluated. X-ray Diffraction (XRD, Bruker D8 Advance, Germany) with Cu-Kα radiation (λ = 1.5406 Å) was used to analyze crystalline phases. X-ray Fluorescence (XRF, PANalytical Axios, Netherlands) determined elemental composition. Surface morphology was examined using Scanning Electron Microscopy (SEM, JEOL JSM-7610F, Japan). The elemental composition and chemical states of the prepared samples were analyzed using X-ray Photoelectron Spectroscopy (XPS, PHI 5000 VersaProbe III; ULVAC-PHI, Inc., Japan) under ultra-high vacuum (~2×10^{-7} Pa). A monochromatic Al Kα X-ray source (hν = 1486.6 eV) was used with a beam diameter of 100 µm. The pass energy was set to 280 eV for survey scans and 55 eV for high-resolution scans, with a step size of 0.05 eV. A raster scan was applied to the as-prepared samples, and the stage tilt angle was fixed at 45°. Charge compensation was achieved using a neutralizer (1.5 V, 20 µA). The base pressure during analysis was maintained at ~8×10^{-8} Pa. Samples were mounted on non-conductive tape. Data acquisition and peak deconvolution were performed using Multipak software.

2.3. Preparation of Heavy Metal Stock Solutions

All chemicals used in this study were of analytical grade (≥99.5%, 200 mesh) and were procured from Merck and Sigma-Aldrich. The required masses of potassium dichromate (K2Cr2O7), cadmium nitrate [Cd(NO3)2], and lead nitrate [Pb(NO3)2] were accurately weighed and **dissolved together in distilled water** (resistivity ≥15 MΩ·cm) to prepare a **mixed heavy-metal stock solution** containing 50mg/l for Cr(VI) and Cd(II), and 10 mg/l for Pb(II). The exact mass of each metal salt was calculated. All experiments were performed at room temperature (298 ± 2 K) under atmospheric pressure. The pH of the solutions was adjusted using hydrochloric acid (HCl) or sodium hydroxide (NaOH) wherever required.

2.4. Adsorption Experiments

Batch adsorption experiments were carried out by adding a known mass of the Fe_3O_4/TiO_2–banana peel nanocomposite (0.5–2.5g) into a series of 250 mL conical flasks containing 100 mL of the mixed heavy-metal solution (V, mL) with an initial concentration of 50 mg/L (C_o). The flasks were placed on a magnetic stirrer and agitated at 90 rpm for a contact time of 60 min to allow adsorption to occur. After each run, the supernatant was withdrawn, filtered through Whatman No. 42 filter paper, and the residual concentrations of Cr (VI), Cd (II), and Pb (II) (C_t) were analyzed using Atomic Absorption Spectroscopy (AAS).

The amount of metal ions adsorbed, denoted as qt (mg/g), was calculated using Eq. 2 (Otieno et al. 2021)

$$q_t = \frac{(Co-Ct)}{W} V \qquad (1)$$

where C0 and Ct are the metal ion concentrations (mg/L) initially and at the end of the run, respectively; V is the solution volume (mL); and W is the mass of the adsorbent (g).

2.5. Adsorption isotherms

Adsorption isotherms were used to evaluate the equilibrium data from the batch experiments. The equilibrium data were analyzed using the nonlinear **Langmuir** and the **Freundlich** isotherm models (Eq. 2 and 3). The nonlinear form of the isotherms was preferred over the linearized equations to minimize errors associated with data transformation and to provide more accurate and reliable parameter estimation.

The **Langmuir isotherm model** assumes monolayer adsorption onto a homogeneous surface with finite, identical active sites, and is expressed as:

$$q_e = \frac{q_{max} K_L C_e}{1+K_L C_e} \qquad (2)$$

where:

- qe (mg/g) is the amount of adsorbate adsorbed at equilibrium,
- Ce (mg/L) is the equilibrium concentration of cadmium in solution,
- qmax (mg/g) is the maximum adsorption capacity,
- KL (L/mg) is the Langmuir constant related to adsorption affinity.

The Freundlich model describes multilayer adsorption onto heterogeneous surfaces and is given by:

$$q = K_F C_e^{1/n} \qquad (3)$$

where:

- K_F (mg/g) $(L/mg)^{1/n}$ is the Freundlich constant indicating adsorption capacity,
- n is the heterogeneity factor, with 1/n representing adsorption intensity.

The suitability of each model was assessed by correlation coefficients (R^2) and error functions.

2.6. Adsorption kinetics

Kinetic experiments were conducted to investigate the rate and mechanism of Cr (VI), Cd(II), and Pb(II) adsorption onto the synthesized Fe_3O_4/TiO_2/banana peel nanocomposite. Batch adsorption studies were performed at four adsorbent dosage levels (0.5, 1, 1.5, 2, and 2.5g), while keeping the initial metal ion concentration 50 mg/L for Cr(VI) and Cd(II) and 10 mg/l for Pb(II), solution volume (100 mL), and with the natural pH of the water ranging from 6.0 to 6.5. For each contact time, an identical 250 mL conical flask containing the same solution volume and adsorbent dosage was prepared to maintain constant experimental conditions. The flasks were agitated at 90 rpm using a magnetic stirrer to ensure uniform mixing. At predetermined time intervals ranging from 10 to 120 min, one flask was removed, and the suspension was filtered through Whatman No. 42 filter paper. The residual metal ion concentrations in the filtrate were measured as described in Section 2.4, and the amount of metal adsorbed at time t (qt) was calculated using Equation (1).

$$q_t = q_e\,(1-e^{-k1t})$$

where:

- q_t (mg/g) is the amount of cadmium adsorbed at time ttt,
- q_e (mg/g) is the adsorption capacity at equilibrium,
- k_1 (1/min) is the pseudo-first-order rate constant.

The pseudo-second-order model is given by:

$$q_t = \frac{K_2 q_e^2 t}{1+k_2 q_e t}$$

2.7. Error analysis

To evaluate the accuracy and reliability of the isotherm and kinetic models, the root mean square error (RMSE) was applied to compare the experimental and predicted adsorption capacities. RMSE provides a direct measure of the average deviation between experimental and model-calculated values, offering a more reliable assessment of model performance than the coefficient of determination (R^2) alone. It was calculated using the following equation:

- Root mean square error (RMSE)= $\sqrt{\frac{1}{N}}\sum q_{e,exp-q_{cal}})^{2}$

where and $q_{e,\ exp}$ and $q_{e,\ cal}$ (mg/g) are the experimental and calculated adsorption capacities, respectively, and N is the number of experimental data points. Lower RMSE values indicate better agreement between experimental and predicted results.

3. RESULTS AND DISCUSSION

3.1. Adsorbent Characteristics

The FTIR spectra of banana peel powder (BP), Fe_3O_4, and TiO_2 nanoparticles before and after adsorption are presented in Fig. 2a–b. In the BP spectrum, the broad band around 3400 cm^{-1} corresponds to O–H stretching of hydroxyl groups in cellulose, hemicellulose, and lignin, while the peaks near 2920 cm^{-1} are assigned to aliphatic C–H stretching. The absorption bands at 1655–1560 cm^{-1} and 1250–1020 cm^{-1} represent C=O/C=C and C–O stretching vibrations, respectively, indicating the presence of functional groups capable of binding metal ions.

The Fe3O4 spectrum shows a broad O–H band at ~3400 cm^{-1} and a strong Fe–O stretching vibration between 550–480 cm^{-1}, confirming the formation of magnetite nanoparticles. TiO_2 displays characteristic Ti–O–Ti and Ti–O vibrations at ~745 cm^{-1} and 480–500 cm^{-1}, respectively, verifying its crystalline structure.

After adsorption, the Fe_3O_4/TiO_2/BP nanocomposite spectrum exhibits noticeable changes in band intensity and position. The broad O–H band (3759–3402 cm^{-1}) becomes less intense and slightly shifted, indicating the participation of hydroxyl groups in metal binding through hydrogen bonding or ion exchange. The peaks at 1658 cm^{-1}, 1407 cm^{-1}, and 1257 cm^{-1} correspond to C=O, carboxylate, and C–O vibrations, suggesting their involvement in complexation with metal ions. The persistence of Fe–O and Ti–O bands (1000–750 cm^{-1}) confirms that the structural framework of the composite remained stable after adsorption.

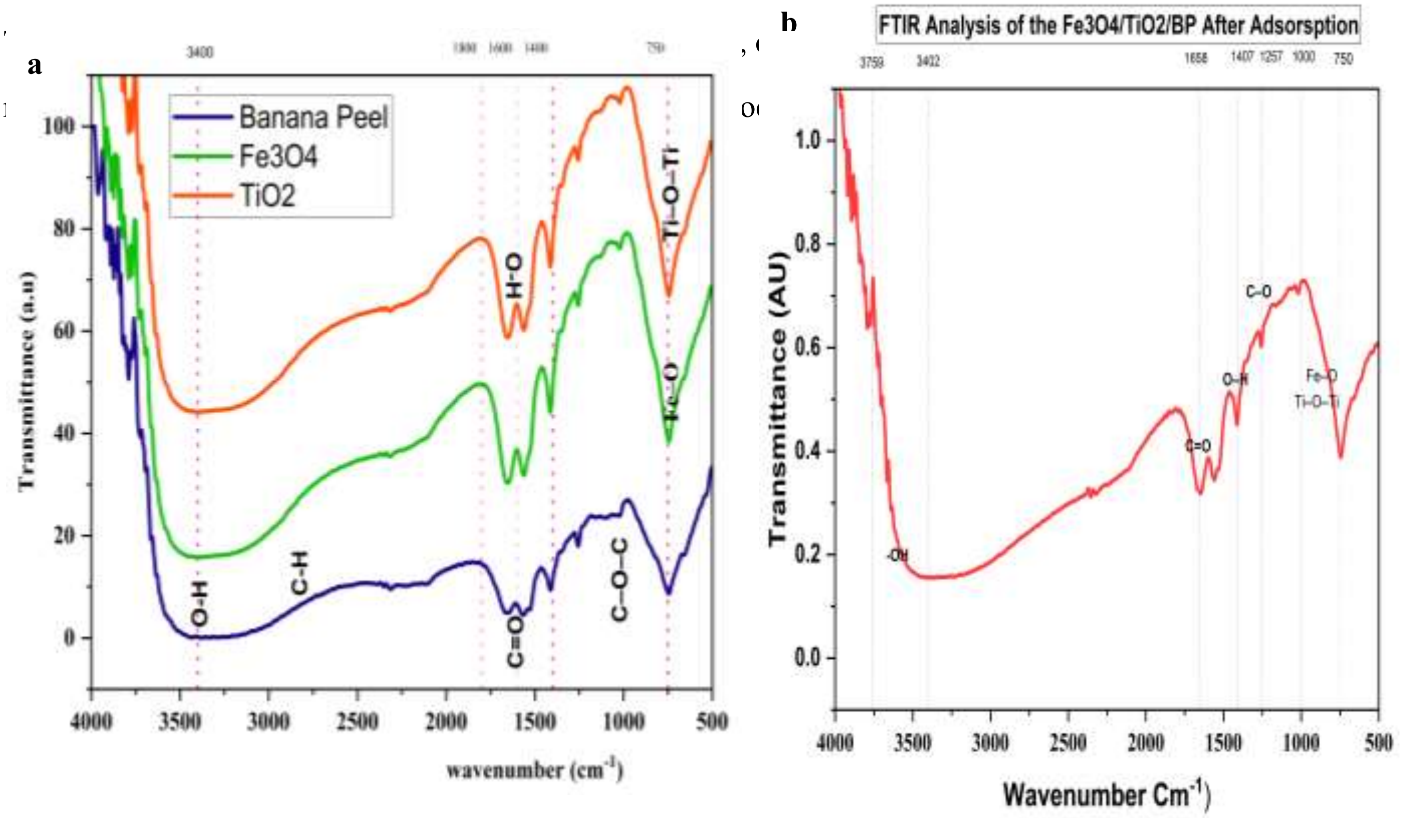

Fig. 2: FTIR spectrum of the materials (a) before adsorption, (b) after adsorption.

The XPS analysis of iron oxide (Fig. 3a–b) shows clear contributions from Fe^{2+} $2p^{3/2}$ (~708.5 eV) and Fe^{3+} $2p^{3/2}$ (~712.0 eV), along with their spin–orbit partners ($\Delta E \approx 13.1$ eV; 2:1 ratio). Shake-up satellite peaks are also observed at approximately 716 eV and 719 eV. All binding energies were calibrated against the C 1s peak at 285.0 eV, and the fitted parameters are summarized in Table 1.

The O 1s spectrum (Fig. 3b) was deconvoluted into three components: lattice oxygen (O^{2-}, ~529.3 eV), hydroxyl groups or oxygen vacancies (~531.9 eV), and adsorbed water/organic species (~532.7 eV).

Survey scans confirmed the presence of C 1s, Fe 2p, O 1s, S 2p, and Ti 2p regions in both the iron oxide and banana peel-derived samples. The Fe 2p doublets of an Fe_2O_3 standard were used as reference peaks for determining the oxidation state.

The XPS results confirm the coexistence of Fe^{2+} and Fe^{3+} species, together with surface hydroxyl and oxygen defect sites, which are expected to play a crucial role in adsorption and surface reactivity (Table 1).

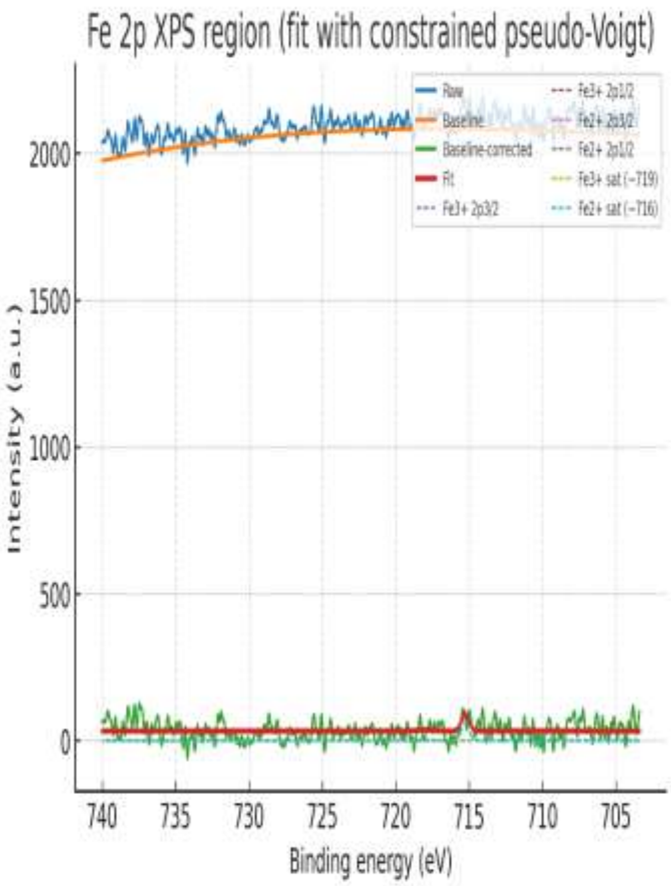

Fig. 3a: Fe 2p XPS region of iron oxide.

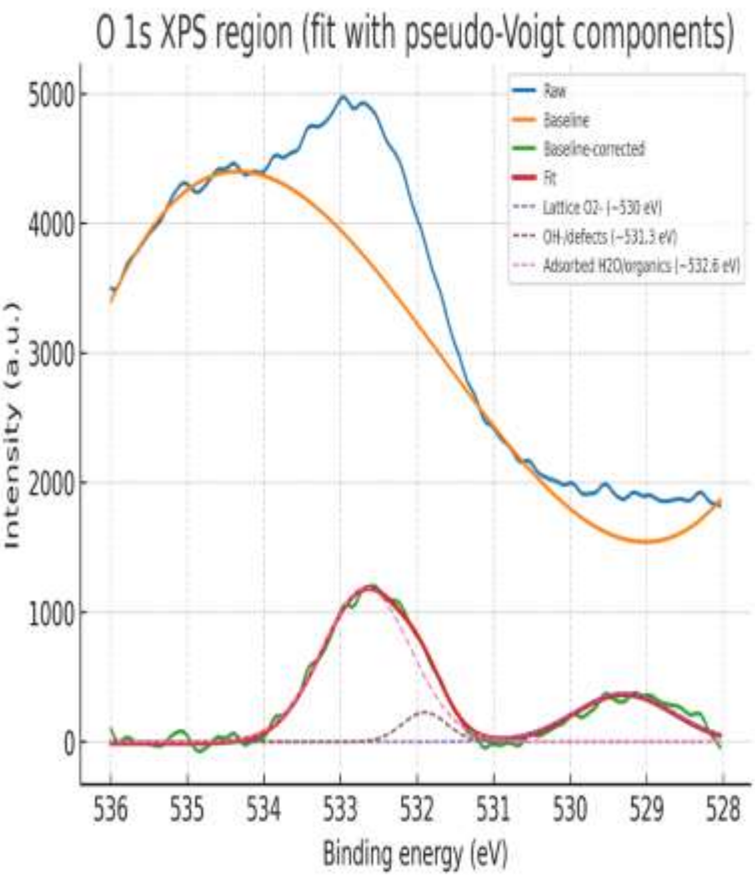

Fig. 3b: O1s XPS region of iron oxide.

Table 1: Fitted parameters of XPS analysis on iron oxide.

Component	Area (a.u.)	Position (eV)	Sigma (eV)	Eta (0-1)	Fe^{3+} fraction (from 2p3/2)
Fe^{3+} 2p3/2	1.3E-12	711.9803	1.799834	0.999183	4.88E-07
Fe^{3+} 2p1/2	6.51E-13	725.0803	1.799834	0.999183	4.88E-07
Fe^{2+} 2p3/2	2.67E-06	708.5125	1.773371	0.970402	4.88E-07
Fe^{2+} 2p1/2	1.33E-06	721.6125	1.773371	0.970402	4.88E-07
Fe^{3+} sat	5.626487	718	0.434943	1.17E-13	4.88E-07
Fe^{2+} sat	37.82937	715.2522	0.260823	4.59E-31	4.88E-07

The particle size distribution of the synthesized iron oxide (Fe_3O_4) was analyzed using a HORIBA SZ-100 nanoparticle analyzer (HORIBA Scientific, Japan) based on dynamic light scattering (DLS). Measurements were performed in a transparent four-sided cuvette with a 10 mm optical path length. As shown in Fig. 4, the intensity-weighted particle size distribution exhibits a broad and multimodal profile, indicating the presence of aggregated particles in aqueous suspension. A prominent intensity peak is observed at approximately 1593 nm, while additional contributions at larger sizes suggest the formation of particle agglomerates. The Z-average hydrodynamic diameter (~3432 nm) is considerably higher than the modal size, reflecting the strong sensitivity of the cumulant-based DLS analysis to larger aggregates. The calculated polydispersity index (PDI = 0.67) confirms that the system is highly polydisperse. Although the Fe_3O_4 material consists of nanoscale primary particles, strong magnetic dipole–dipole interactions promote aggregation in aqueous media, and therefore the particle sizes measured by DLS correspond to the hydrodynamic diameters of aggregated clusters rather than the intrinsic nanoscale dimensions of the primary particles.

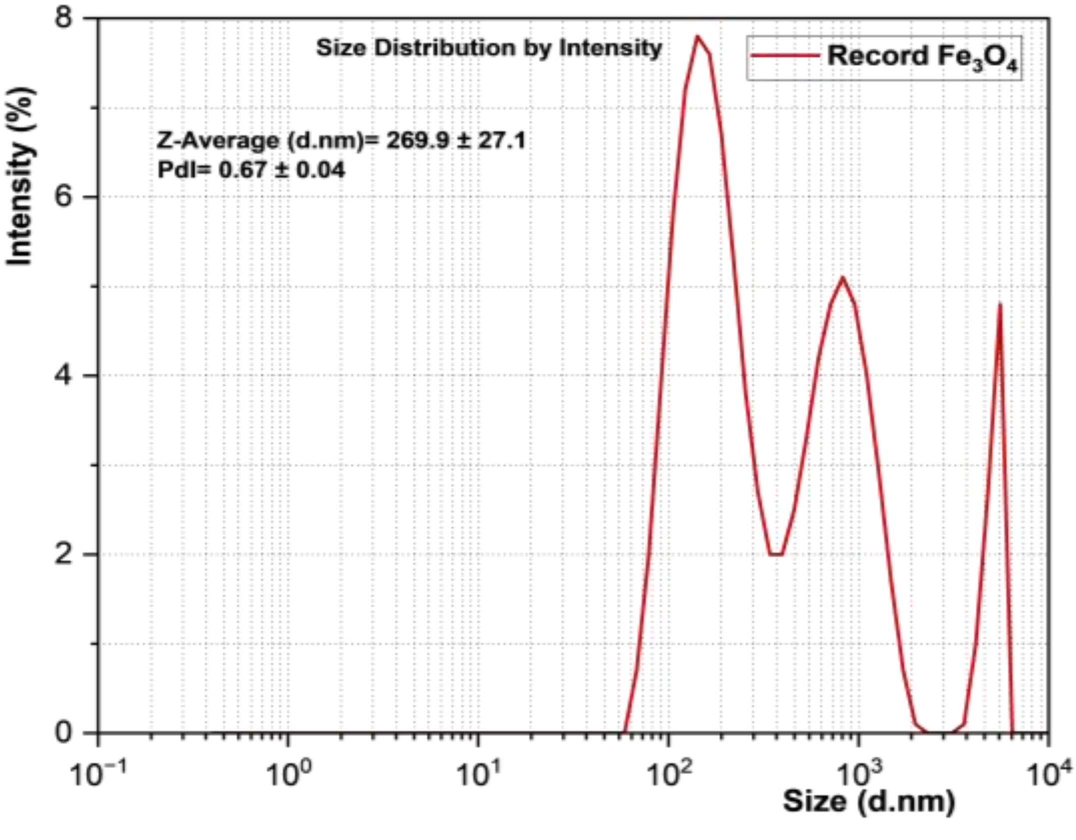

Fig. 4: Particle size distribution curve of iron oxide measured by Dynamic Light Scattering.

The surface morphology of the synthesized iron oxide (Fig. 5a–d) shows predominantly irregular and agglomerated particles, which is a common characteristic of nanoscale iron oxides resulting from strong magnetic interactions and high surface energy. At higher magnifications, SEM images reveal that these agglomerates are composed of fine primary nanoparticles with dimensions in the nanoscale, clustered into larger secondary aggregates.

This observation reconciles the SEM and DLS results, as SEM provides information on the morphology and size of primary particles in the dry state, whereas DLS measures the hydrodynamic diameter of particle agglomerates in suspension. The presence of nanoscale primary particles contributes to a high effective surface area, which is advantageous for adsorption processes.

EDS analysis (Fig. 5e) confirms the presence of Fe and O as the main elements, consistent with iron oxide formation. Minor carbon peaks are attributed to residual organics or carbon coating used during SEM preparation. The absence of significant impurity peaks indicates high material purity.

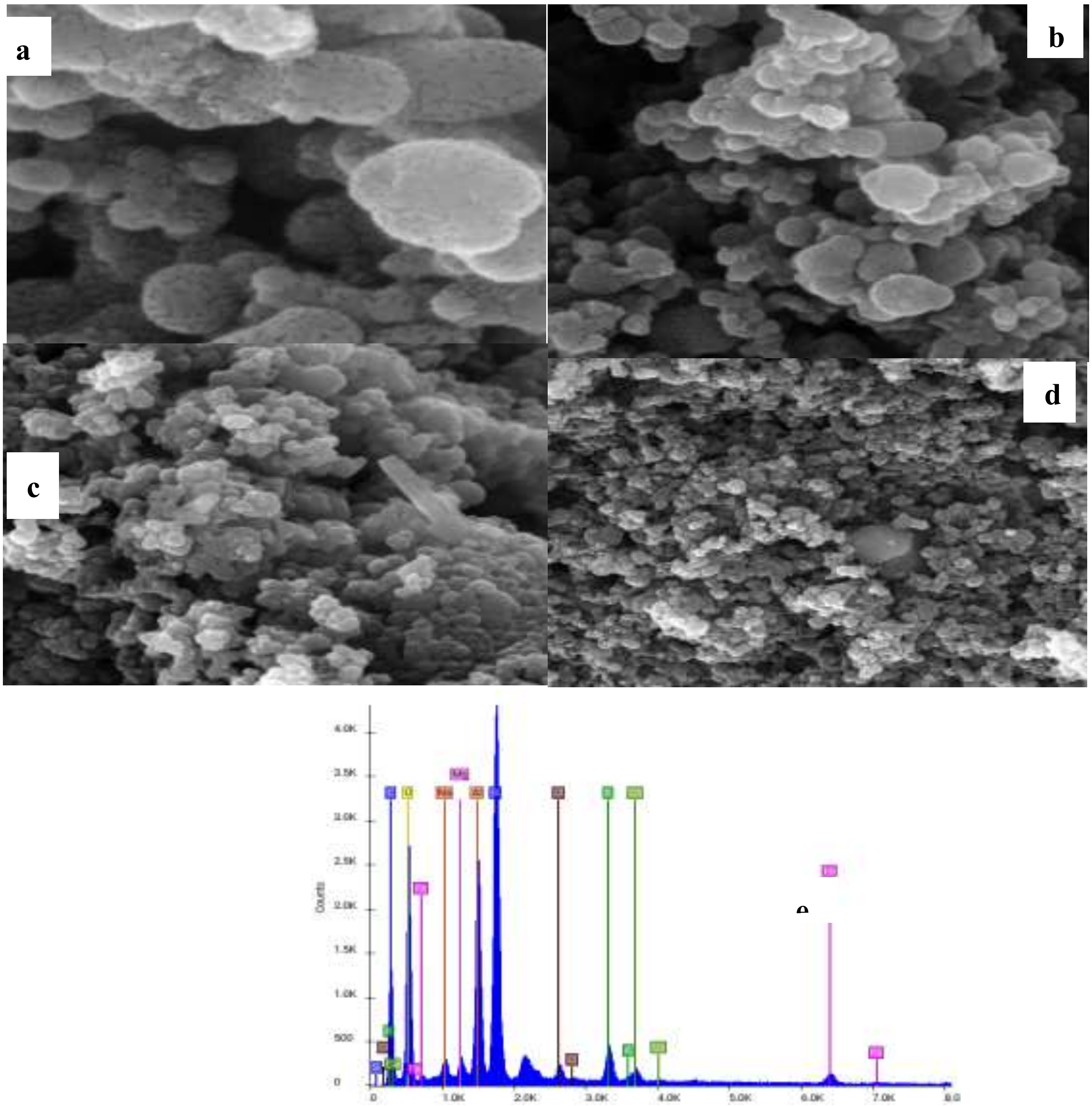

Fig. 5a-e: Scanning Electron Microscopy of Iron oxide.

The SEM images (Fig. 6a–e) illustrate that the synthesized TiO_2 particles exhibit irregularly shaped morphologies, predominantly consisting of rod-like and granular structures with rough surfaces. The particles are densely packed and tend to aggregate into clusters, which is characteristic of TiO_2 nanoparticles due to their high surface energy. The micrographs also show variations in particle size, suggesting polydispersity within the sample (Suttiponparnit et al. 2011). The EDS spectrum (Fig. 6f) confirms the presence of titanium (Ti) and oxygen (O) as the principal elements, consistent with the formation of TiO_2. Minor peaks of elements such as C, Na, and Si are also observed, which may originate from the supporting substrate, residual precursor materials, or surface contaminants. These results collectively verify the successful synthesis of TiO_2 nanoparticles with nanostructured morphology and characteristic elemental composition suitable for adsorption applications.

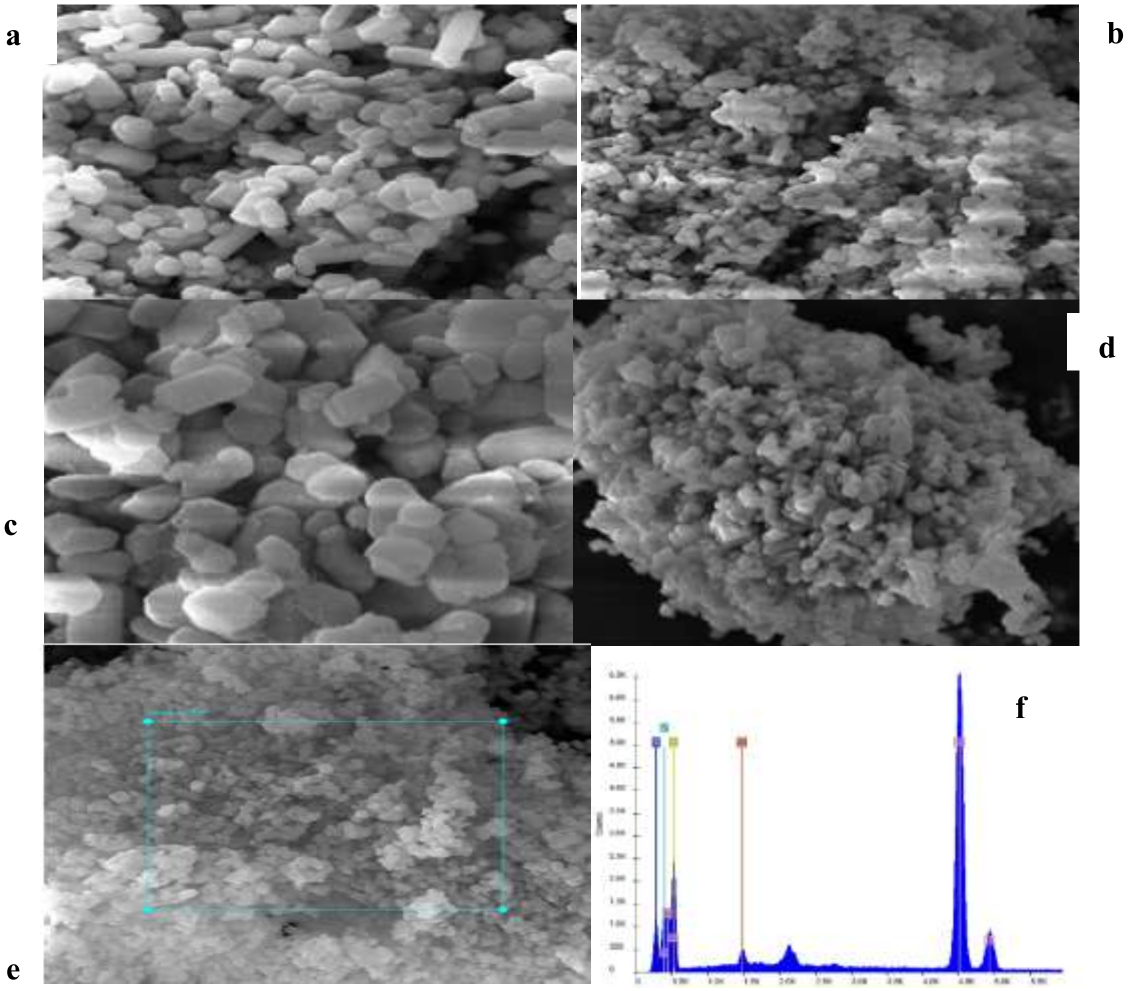

Fig. 6. SEM micrographs and EDS spectrum of Titanium dioxide (TiO_2) adsorbent.

The SEM images of banana peel (Fig. 7a–c) show a heterogeneous, rough, and fibrous surface typical of lignocellulosic biomass. The micrographs reveal layered and wrinkled textures with porous and fibrillar networks, indicating abundant cavities and irregular channels that serve as potential adsorption sites. These morphological features, together with the measured surface area of approximately 13 m^2/g, enhance the accessibility of active sites and facilitate pollutant diffusion within the adsorbent matrix.

The EDS spectrum (Fig. 7d) confirms carbon (C) and oxygen (O) as the dominant elements, consistent with cellulose, hemicellulose, and lignin components, along with minor inorganic elements originating from the natural biomass or introduced during activation.

The SEM–EDS results demonstrate that the banana peel-based adsorbent possesses a rough, porous morphology, moderate surface area, and diverse elemental composition, making it an efficient and sustainable material for adsorption and water purification applications.

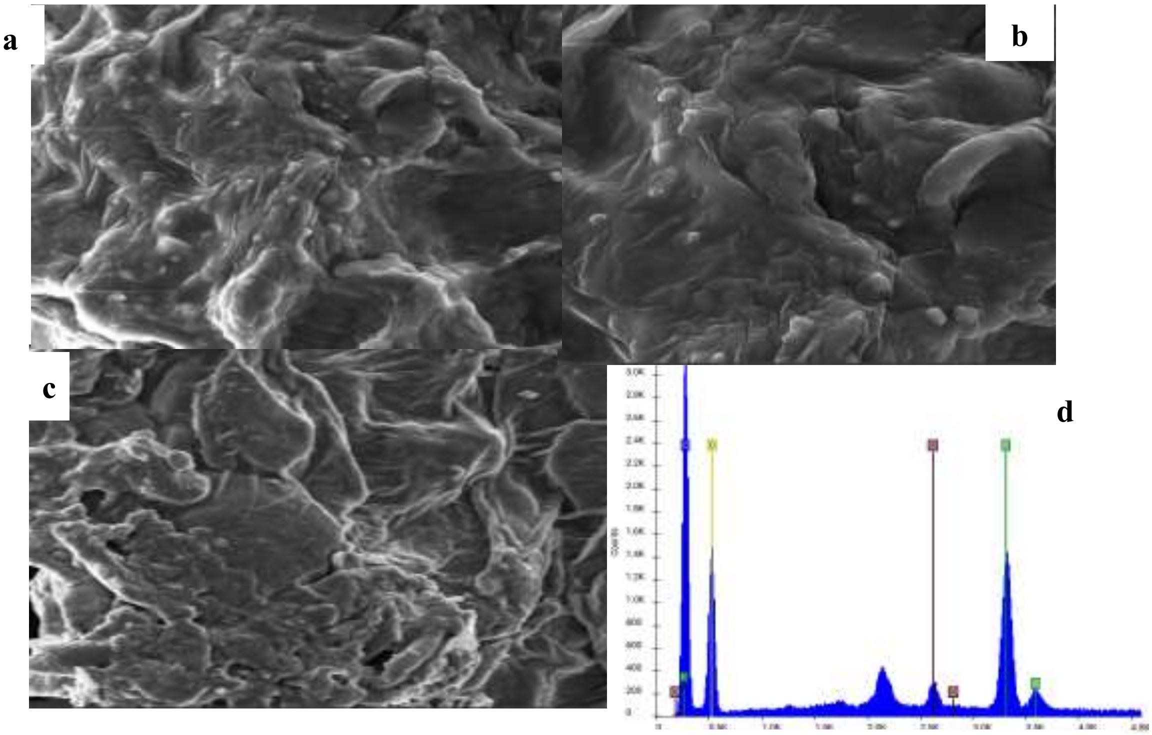

Fig. 7a-d. SEM micrographs and EDS spectrum of banana peel (BP)-based adsorbent.

3.1.4. Surface area and porosity analysis (BET/BJH)

The surface area and pore characteristics of Fe_3O_4, TiO2, and banana peel were evaluated by nitrogen adsorption–desorption (BET/BJH) analysis at 77 K (Fig. 8). The adsorption–desorption isotherms exhibit type IV behavior with hysteresis loops, indicating the presence of mesoporous structures.

Fe_3O_4 displayed a high BET surface area of 342.10 m^2/g, with a total pore volume of 0.432 cm^3/g and an average pore diameter of 2.94 nm, confirming its mesoporous nature with nanoscale features. TiO_2 showed a surface area of 172.44 m^2/g, a pore volume of 0.448 cm^3/g, and an average pore diameter of 9.96 nm, also within the mesoporous range. In contrast, banana peel exhibited a much lower surface area (22.94 m^2/g) and pore volume (0.019 cm^3/g), consistent with its biomass-derived structure.

The high surface areas and nanoscale pore dimensions of Fe_3O_4 and TiO_2 support the presence of nanoscale primary particles observed by SEM. .

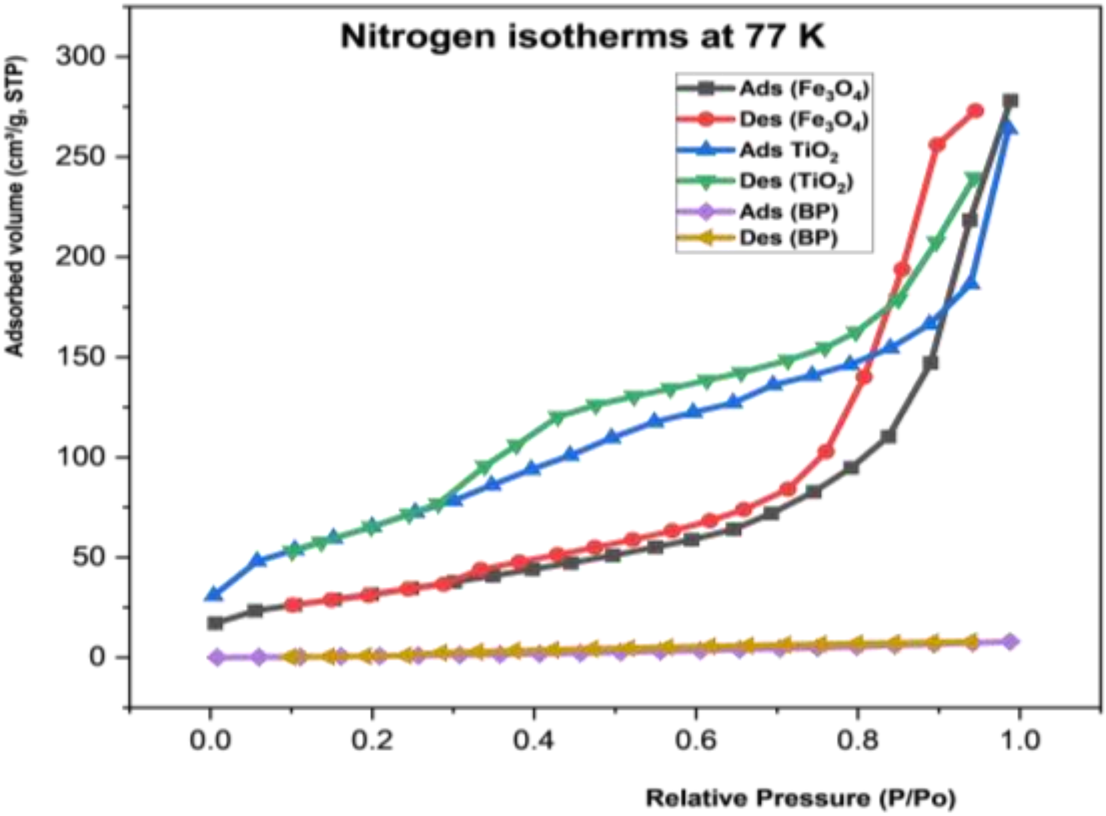

Fig 8: N_2 adsorption-desorption isotherms and BJH/BET textural parameters of the materials at 77 K.

3.1.5-Zeta potential

Zeta potential analysis was conducted to assess the surface charge properties and colloidal stability of the adsorbent materials. As shown in the Fig. 9 banana peel (BP) had a strongly negative zeta potential of −29.2

mV, indicating good electrostatic stability in aqueous suspension, which can be linked to the presence of abundant oxygen-containing functional groups such as carboxyl and hydroxyl groups. In contrast, TiO_2 and Fe_3O_4 displayed low positive zeta potential values of +7.21 mV and +13.5 mV, respectively, indicating limited colloidal stability and a greater tendency for particle aggregation in water. The higher magnitude of negative surface charge observed for BP emphasizes its potential to enhance surface stability and adsorption performance when used as a composite component with inorganic nanoparticles. These results support the use of banana peel as a biopolymeric modifier to improve the dispersion behavior and electrostatic properties of Fe_3O_4- and TiO_2-based adsorbents for water and wastewater treatment applications.

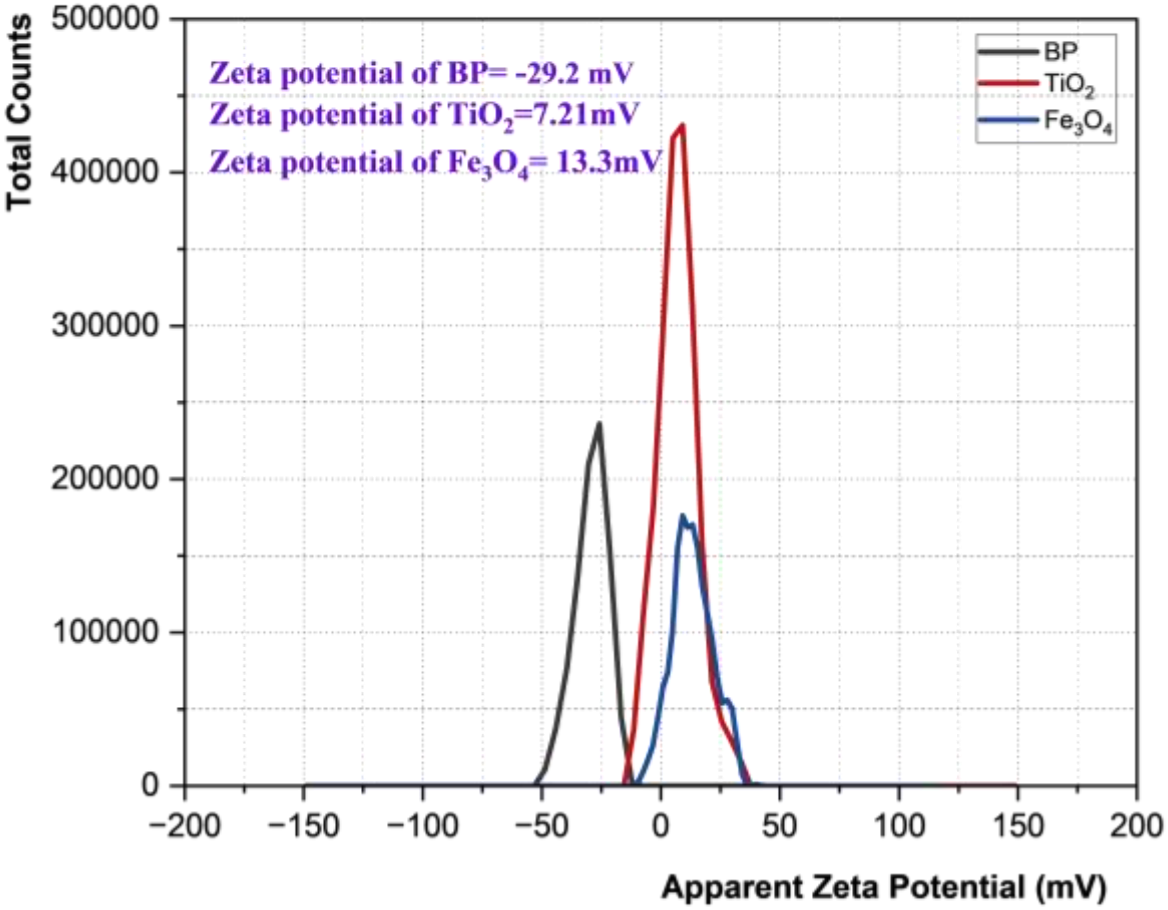

Fig. 9: Zeta potential distribution of $Fe_3O_4/TiO_2/BP$ nanoparticles.

3.1.6. VSM analysis

The magnetic properties of the iron oxide and TiO_2 were investigated using a vibrating sample magnetometer (VSM). The hysteresis loop of iron oxide (Fig. 10) exhibits a narrow S-shaped curve with low coercivity (Hc ≈ 80–120 Oe) and very low remanent magnetization (Mr ≈ 5–10 × 10^{-5} emu/g), indicating weak ferrimagnetic behavior. The saturation magnetization was determined to be approximately 0.0025 emu/g.

The low Ms value indicates that the magnetic response of the material is weak, likely due to surface modification and dilution of the magnetic phase within the composite. Consequently, the material exhibits limited magnetic responsiveness rather than practical magnetic separability, and magnetic recovery would only be possible under strong external magnetic fields applied in proximity (Selim et al. 2023).

In contrast, TiO_2 exhibits an almost linear magnetization curve with negligible coercivity and remanence, confirming its nonmagnetic nature. Although TiO_2 does not contribute to magnetic behavior, its incorporation enhances the adsorption performance of the composite material.

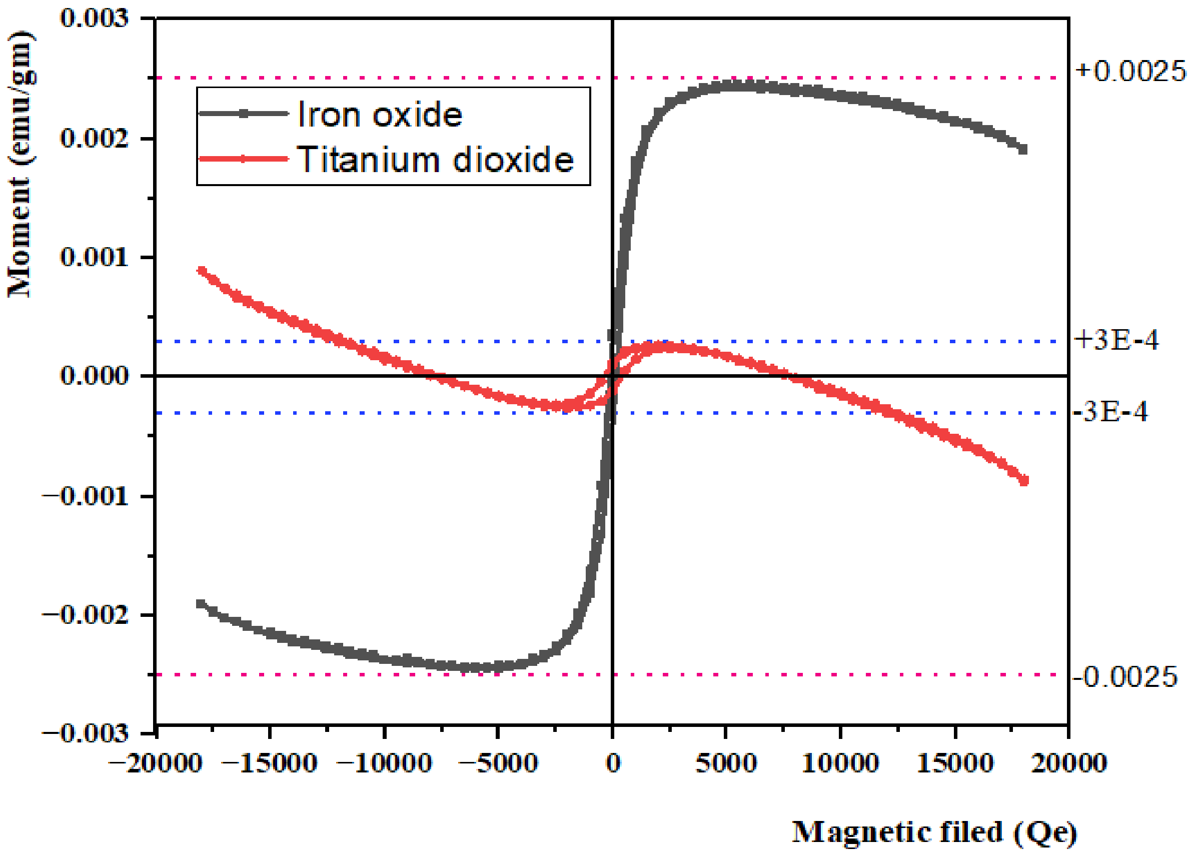

Fig. 10: VSM analysis of iron oxide and titanium dioxide.

3.2. Adsorption isotherms

The equilibrium adsorption data were fitted using nonlinear Langmuir, Freundlich, Temkin, and Redlich–Peterson isotherm models (Fig. 11a–e, Table 2) to explore the adsorption behavior of Cr(VI), Cd(II), and Pb(II) onto the Fe_3O_4/TiO_2/banana peel nanocomposite. Adsorption efficiency increased with adsorbent dosage and reached an optimum at 2.0 g, reflecting an increase in the number of available active sites for metal uptake (Foroutan et al. 2022).

For Cr(VI), both the Langmuir ($R^2 = 0.729$, qmax = 14.40 mg/g) and the Freundlich ($R^2 = 0.75$, KF = 7.12, 1/n = 0.47) models provided moderate fits, indicating a mixed adsorption behavior involving partial monolayer coverage on a heterogeneous surface. The Freundlich constant (1/n < 1) suggests favorable adsorption. The Redlich–Peterson model ($R^2 = 0.73$, $\beta = 0.51$) further supports this mixed adsorption mechanism.

In the cases of Cd(II) and Pb(II), all tested models for Cd(II) exhibited low correlation coefficients ($R^2 \leq 0.20$), while several models for Pb(II) yielded statistically invalid fits, including negative R^2 values. These outcomes result from near-complete (~100%) removal efficiencies achieved during the experiments, which led to equilibrium concentrations approaching zero. Under such conditions, conventional adsorption isotherm models cannot be reliably fitted due to the absence of a well-defined equilibrium curve. Consequently, no definitive adsorption mechanisms can be inferred for Cd(II) or Pb(II) based on the applied isotherm models, and the estimated model parameters should be interpreted with caution.

Overall, only Cr(VI) adsorption could be reasonably described by conventional isotherm models (Langmuir and Freundlich), whereas Cd(II) and Pb(II) exhibited adsorption behaviors beyond the applicability of the tested isotherm models.

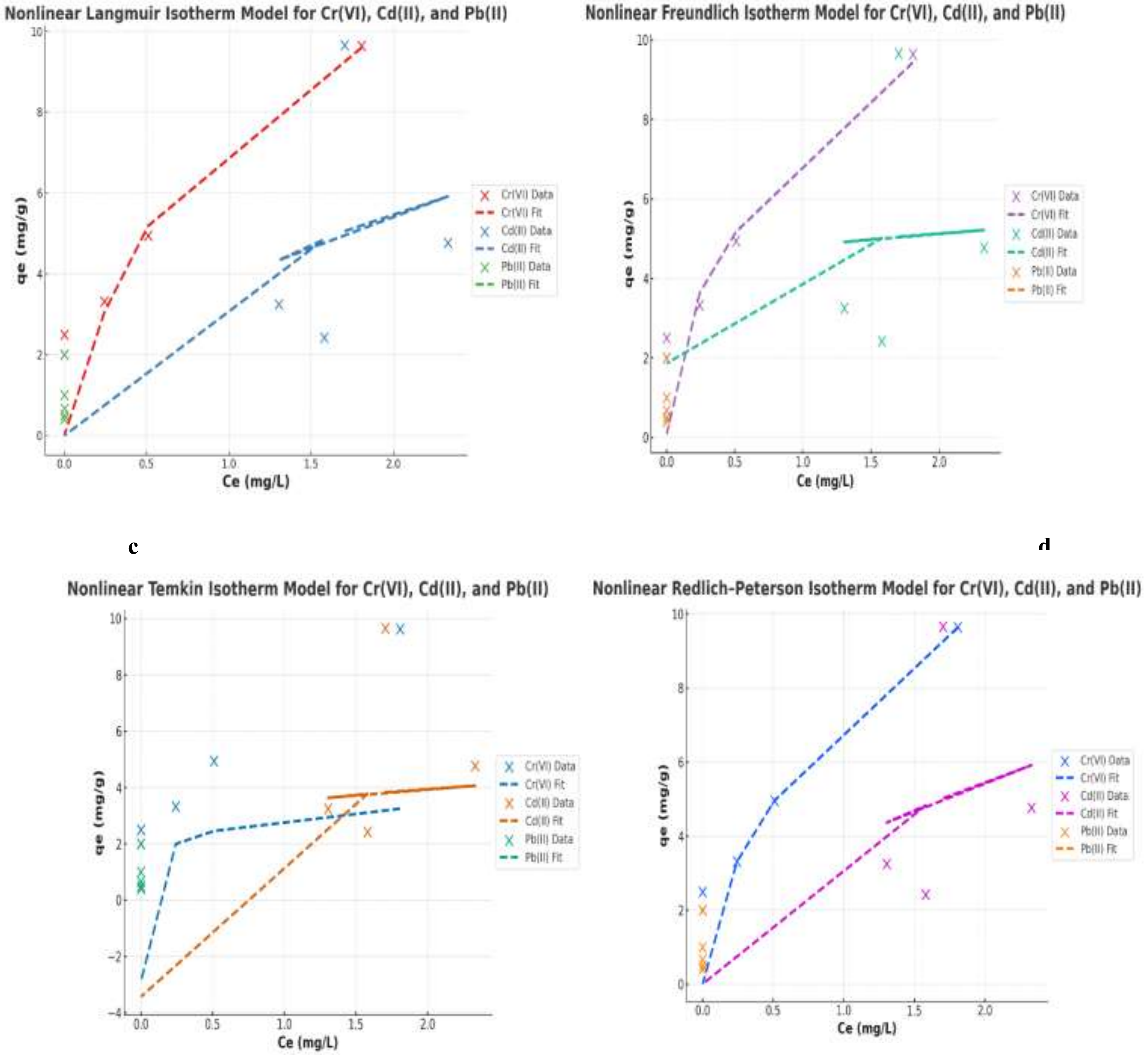
Nonlinear Langmuir Isotherm Model for Cr(VI), Cd(II), and Pb(II)

Nonlinear Freundlich Isotherm Model for Cr(VI), Cd(II), and Pb(II)

Nonlinear Temkin Isotherm Model for Cr(VI), Cd(II), and Pb(II)

Nonlinear Redlich-Peterson Isotherm Model for Cr(VI), Cd(II), and Pb(II)

Fig. 11: Adsorption isotherm models (a-Nonlinear Langmuir, b-Nonlinear Freundlich, Nonlinear Temkin, and d-Nonlinear Redlich–Peterson) for metal ions removal onto Fe_3O_4/TiO/BP.

Table 2: Adsorption isotherm models and their parameters.

Model	Metal	Model Parameters	R^2	RMSE
Langmuir	Cr(VI)	Q_{max} = 14.3983 mg/g; K_L = 1.10588 L/mg	0.729	1.44
	Cd(II)	Q_{max} = 10.966 mg/g; K_L = 0.50213 L/mg	0.134	2.59
	Pb(II)	Q_{max} = 100 mg/g; K_L = 10 L/mg	-1.966	0.99
Freundlich	Cr(VI)	K_F = 7.12; 1/n = 0.47	0.75	1.39
	Cd(II)	K_F = 4.78; 1/n = 0.102	0.20	2.49
	Pb(II)	K_F = 27.15; 1/n = 0.37	2.22E–	0.58
Temkin	Cr(VI)	AT = 100 L/g; bT = 3962.954 J/mol	-1.65	4.51
	Cd(II)	AT = 100 L/g; bT = 3320.767 J/mol	-0.70	3.63
	Pb(II)	AT = 100 L/g; bT = 10000 J/mol	-12.53	2.13
Redlich–Peterson	Cr(VI)	KR = 100 L/g; aR = 13.10 L/mg; β = 0.51	0.73	1.43
	Cd(II)	KR = 100 L/g; aR = 25.34 L/mg; β = 0.49	0.13	2.60
	Pb(II)	KR = 100 L/g; aR = 2.99E–05 L/mg; β = 1	-2.42	1.07

It should be noted that the adsorption experiments were conducted in a multicomponent system in which Cr(VI), Cd(II), and Pb(II) coexisted in solution and competed for the same surface-active sites of the Fe_3O_4/TiO_2/BP nanocomposite. Therefore, their adsorption behaviors are interdependent and cannot be interpreted as equivalent to single-metal systems. The observed differences in removal efficiency can be attributed to variations in ionic charge, hydrated ionic radius, polarizability, and aqueous speciation. Pb(II) exhibited the highest affinity toward the adsorbent, followed by Cd(II), while Cr(VI), predominantly present as anionic species, showed comparatively weaker competitive adsorption. Although the isotherm models were assessed individually for clarity, the results reflect competitive adsorption behavior under multicomponent conditions. Quantitative competitive adsorption modeling was beyond the scope of this study and warrants further investigation.

3.3. Kinetic Studies

The effect of adsorbent dosage on adsorption kinetics was assessed to reflect practical operating conditions rather than to determine intrinsic kinetic constants. As the adsorbent dosage increased, the adsorption capacity, expressed in mass units (qe, mg/g), decreased, which can be attributed to a dilution effect and partial underutilization of the available surface-active sites at higher doses. This behavior is common in batch adsorption systems and does not indicate a decline in adsorption efficiency or rate.

The kinetic parameters obtained at different adsorbent dosages are not directly compared as intrinsic constants. Instead, kinetic modeling was employed to describe adsorption trends and rate-controlling processes independently at each dosage condition

3.3.1. Kinetic Studies for Chromium (Cr(VI))

The adsorption kinetics of Cr(VI) onto the Fe_3O_4/TiO_2/BP nanocomposite were investigated to understand the rate-controlling processes of ion removal. The adsorption capacity increased rapidly during the initial contact period (10–45 min), which can be attributed to the availability of abundant surface-active sites and favorable electrostatic interactions between Cr(VI) anions and the positively charged surface of the composite. As adsorption progressed, the uptake rate gradually decreased, reaching equilibrium as the available surface-active sites became increasingly occupied relative to the solute concentration, which reduced the driving force for mass transfer.

The kinetic data were analyzed using pseudo-first-order (PFO) and pseudo-second-order (PSO) models (Fig. 12; Table 3). The PSO model provided a better description of the experimental data, as indicated by higher correlation coefficients ($R^2 = 0.84–0.97$) and lower RMSE values compared to the PFO model. This suggests that the adsorption rate is predominantly governed by surface-related interactions and the availability of active sites rather than by diffusion alone.

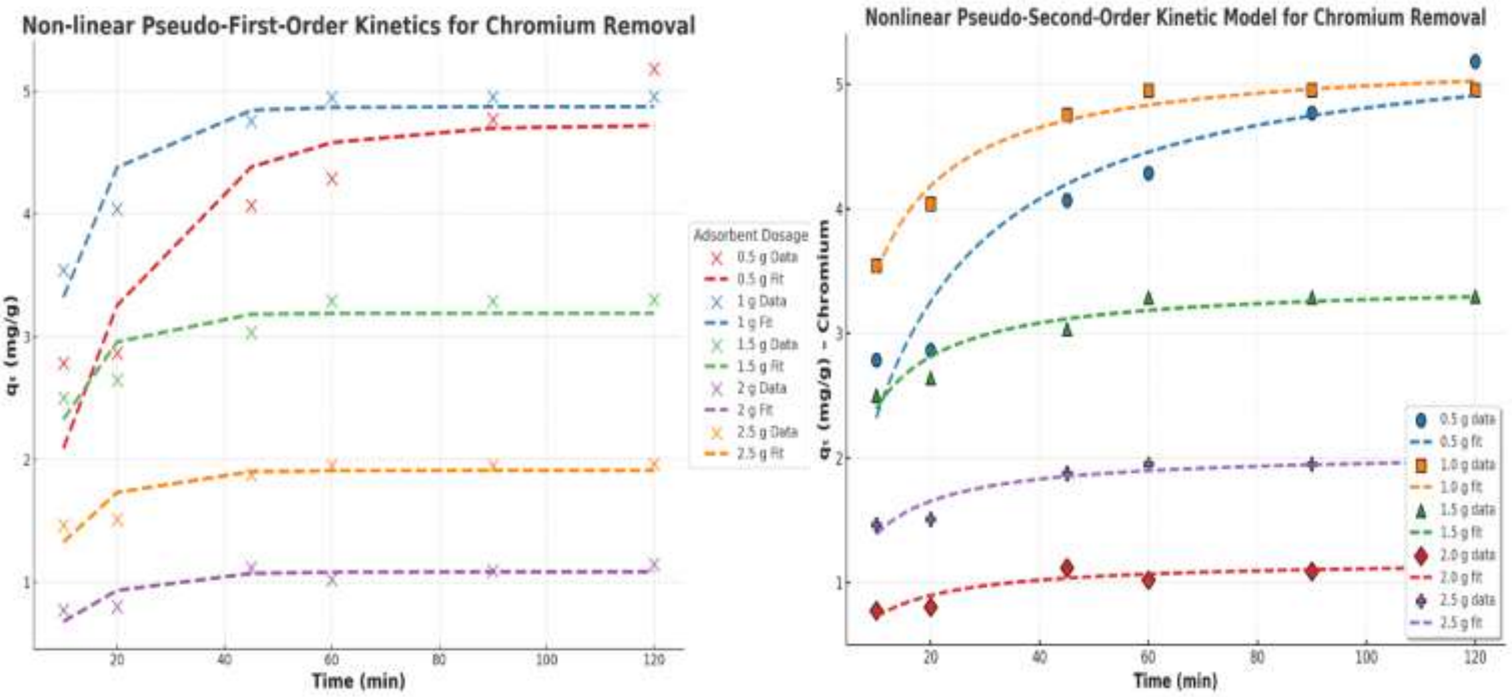

Fig. 12: Nonlinear pseudo first and pseudo second order for chromium removal.

Table 3: Nonlinear fitted pseudo-first-order and pseudo-second-order kinetic models for the removal of Chromium ions using different masses of Fe_3O_4/TiO_2 /BP.

	Pseudo-first-order				**Pseudo-second-order**			
Mass	**qe (mg/g)**	**k1 (1/min)**	**R^2**	**RMSE**	**qe (mg/g)**	**k2**	**R^2**	**RMSE**
0.5g	4.723	0.0584	0.785	0.416	5.46	0.013	0.90	0.286
1g	4.873	0.114	0.893	0.179	5.24	0.038	0.97	0.086
1.5g	3.191	0.131	0.712	0.174	3.41	0.07	0.91	0.1
2g	1.084	0.098	0.735	0.077	1.18	0.133	0.84	0.06
2.5g	1.91	0.118	0.73	0.111	2.05	0.10	0.89	0.071

3.3.2. Kinetic Studies for cadmium (II)

The time-dependent adsorption of Cd(II) onto Fe_3O_4/TiO_2/BP was examined to evaluate the adsorption rate and controlling processes. Rapid adsorption occurred within the first 20–40 min, corresponding to the occupation of the surface-active sites. As equilibrium was approached, the adsorption rate slowed, likely due to site saturation and increased resistance to mass transfer.

Kinetic modeling using the PFO and PSO equations (Fig. 13; Table 4) showed that the PSO model provided a better fit to the experimental data ($R^2 = 0.75$, RMSE = 0.0068) than the PFO model. This indicates that Cd(II) adsorption kinetics are influenced by surface interactions and active-site availability. At higher adsorbent dosages, equilibrium was reached more rapidly, which limited the applicability of kinetic modeling under these conditions.

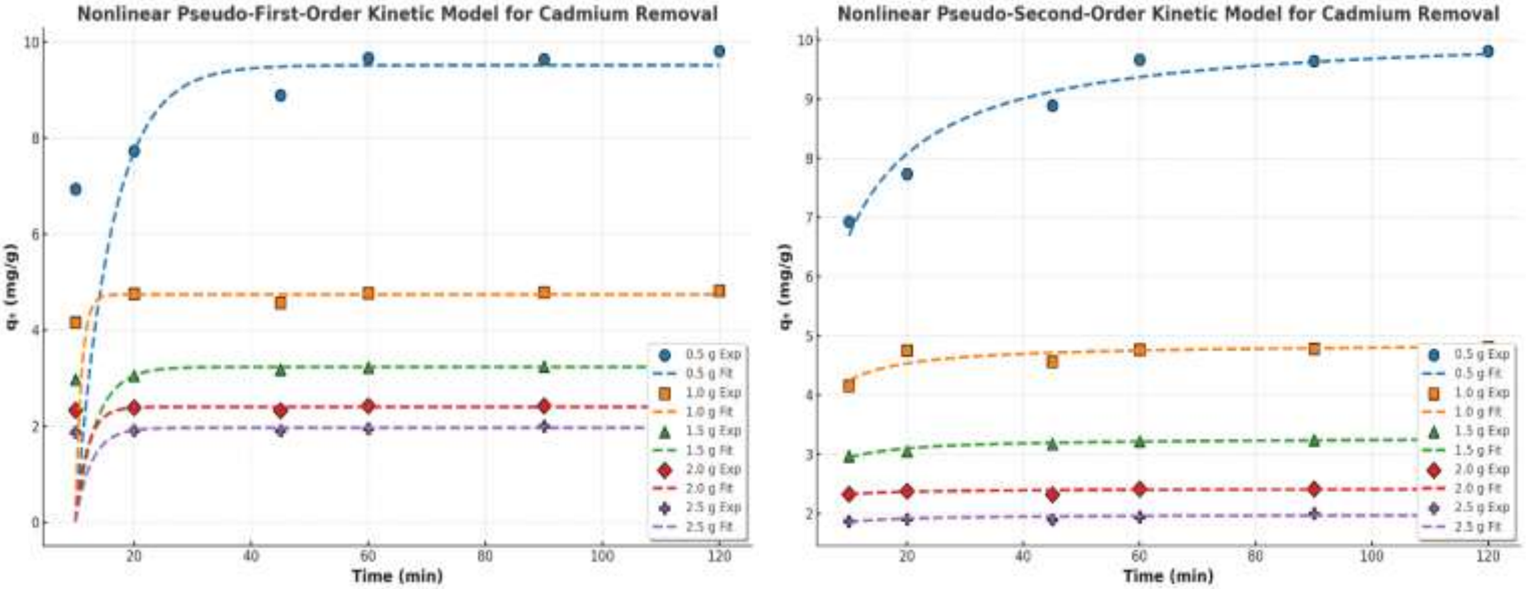

Fig. 13: Nonlinear pseudo first and pseudo second model for cadmium removal.

Table 4: Nonlinear fitted pseudo-first-order and pseudo-second-order kinetic models for the removal of Cadmium ions using different masses of Fe_3O_4/TiO_2 /BP.

	Pseudo-first-order				**Pseudo-second-order**			
Mass	**qe (mg/g)**	**k_1 (1/min)**	**R^2**	**RMSE**	**qe (mg/g)**	**k_2**	**R^2**	**RMSE**
0.5g	9.43	0.11	0.82	0.46	10.18	0.019	0.95	0.23
1g	4.75	0.21	0.86	0.09	4.87	0.14	0.76	0.114
1.5g	3.20	0.25	0.64	0.06	3.28	0.27	0.93	0.028
2g	2.40	0.36	0.29	0.037	2.42	1	0.41	0.034
2.5g	1.95	0.31	0.38	0.04	1.98	0.76	0.63	0.03

3.3.3. Kinetic studies for Lead (Pb(II))

The adsorption of Pb(II) onto the Fe_3O_4/TiO_2/BP nanocomposite exhibited a rapid initial uptake followed by a slower approach to equilibrium. The fast adsorption stage reflects the high affinity of Pb(II) ions for surface-active sites, while the subsequent slower stage may be associated with site saturation and diffusion-related limitations.

Kinetic modeling using the PFO and PSO equations (Fig. 14; Table 5) revealed that the PSO model showed superior agreement with the experimental data, with higher correlation coefficients (R^2= 0.87–0.95) and lower RMSE values. This suggests that Pb(II) adsorption kinetics are primarily controlled by surface interactions rather than by simple physical diffusion.

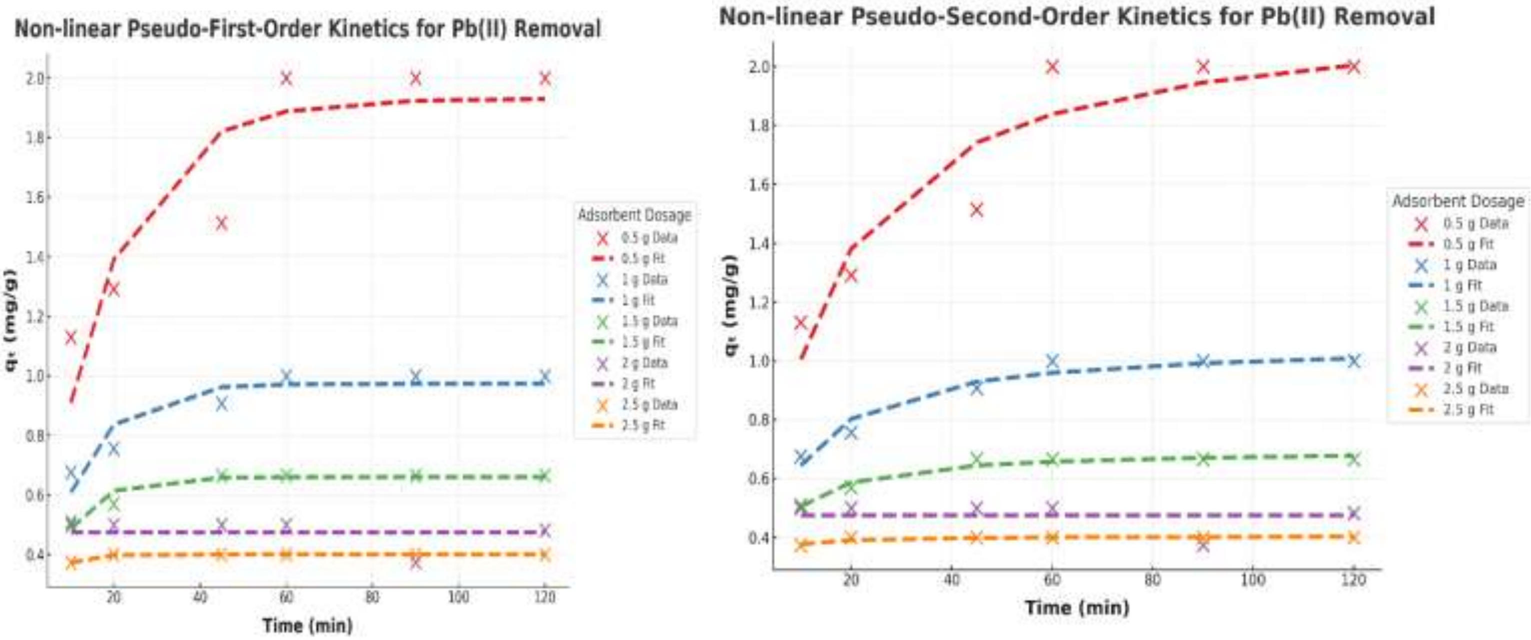

Non-linear Pseudo-First-Order Kinetics for Pb(II) Removal

Non-linear Pseudo-Second-Order Kinetics for Pb(II) Removal

Fig. 14: Nonlinear pseudo first and pseudo second order for lead removal.

Table 5: Nonlinear fitted pseudo-first-order and pseudo-second-order kinetic models for the removal of lead ions using different masses of Fe_3O_4/TiO_2 /BP.

Mass	**Pseudo-first-order**				**Pseudo-second-order**			
	qe (mg/g)	**k_1 (1/min)**	R^2	**RMSE**	**qe (mg/g)**	**k_1 (1/min)**	**R^2**	**RMSE**
0.5g	1.93	0.06	0.78	0.17	2.203	0.038	0.87	0.13
1g	0.97	0.1	0.84	0.05	1.06	0.144	0.95	0.03

1.5g	0.66	0.134	0.88	0.02	0.7	0.37	0.96	0.013
2g	0.48	1	~0.00	0.05	0.51	1	~0.00	0.062
2.5g	0.40	0.27	0.99	0.0006	0.43	3.32	0.808	0.017

Different experimental runs were conducted to compare the effect of adsorbent dosage on the rate of adsorption. The PSO kinetic rate generally increased with the dosage. The equilibrium adsorption capacity for a given adsorbent dosage, as predicted by the PSO model, should be compared to the batch experimental equilibrium data obtained at the same dosage to evaluate the model's accuracy.

The equilibrium adsorption capacities appear to decrease with increasing adsorbent dosage, likely due to the increased availability of sites, given that the initial heavy metal concentration is fixed.

3.4. Comparative Evaluation with Reported Adsorbents

The Fe_3O_4/TiO_2/BP nanocomposite exhibited high adsorption capacities for Cr(VI), Cd(II), and Pb(II), confirming the synergistic effect of Fe_3O_4 and TiO_2 nanoparticles supported on banana peel biomass. The maximum adsorption capacity for Cd(II) (10.9 mg/g) and 100 mg/g for Pb(II) obtained in this study is significantly higher than that of raw banana peel (~5.9 mg/g) reported by (Deshmukh et al. 2017) and comparable to BPB/Fe_3O_4 (~30.3 mg/g) from the same study. It also remains competitive with more advanced composites such as BPAC/Al2O3–Chitosan (~46.9 mg/g) and BPB/Fe_3O_4/ZIF-67 (~50.8 mg/g) reported by (Ramutshatsha-Makhwedzha et al. 2022). Kinetic analysis showed that adsorption followed the pseudo-second-order (PSO) model, particularly at the 2 g dosage, with R^2 values ranging from 0.89 to 0.99 and low RMSE values, indicating predominant chemisorption involving electron exchange or complexation with oxygen-containing functional groups. Compared with Fe_3O_4–Actinomucor sp. composites (qmax = 29.5 mg/g) reported by (Masoudi et al. 2018), the Fe_3O_4/TiO_2/BP nanocomposite demonstrated superior capacity and similar kinetic behavior.

These results confirm that the Fe_3O_4/TiO_2/BP nanocomposite achieves a favorable balance between adsorption efficiency, structural stability, and simple, eco-friendly synthesis, making it a promising low-cost material for heavy metal removal from aqueous systems.

5. CONCLUSIONS

This study successfully synthesized and evaluated a Fe_3O_4/TiO_2/banana peel (BP) nanocomposite for the adsorption of Cr(VI), Cd(II), and Pb(II) from aqueous solutions. Characterization confirmed the presence of functionalized magnetic surfaces with high reactivity and structural stability. Adsorption equilibrium data were best fitted by the Langmuir and Redlich–Peterson models, indicating that metal ions were primarily adsorbed in a monolayer manner on homogeneous active sites. The kinetic data followed the pseudo-second-order model, confirming that the adsorption process was governed by chemisorption involving valence forces or surface complexation. The maximum adsorption capacities obtained, 14.4 mg/g for Cr(VI), 10.9 mg/g for Cd(II), and 100 mg/g for Pb(II), were comparable or superior to those reported for similar nanocomposites. These findings demonstrate that the Fe_3O_4/TiO_2/BP nanocomposite is an efficient, magnetically separable, and environmentally friendly material for heavy metal removal from aqueous systems, with promising potential for practical water treatment applications and sustainable waste utilization

Author Contributions: Conceptualization, Koffi Sossou and Alfred O. Mayabi; Methodology, Zeraebruk Negusse Kahsay and Charles K. Cheruiyot**;** Data curation, Zeraebruk Negusse Kahsay; Formal analysis, Charles K. Cheruiyot; Writing – original draft, Koffi Sossou; Supervision, Alfred O. Mayabi, Zeraebruk Negusse Kahsay, Charles K. Cheruiyot.

Funding: This research was funded by the African Union Commission.

REFERENCES

Deshmukh, P. D., Khadse, G. K., Shinde, V. M., & Labhasetwar, P. (2017). Cadmium Removal from Aqueous Solutions Using Dried Banana Peels as An Adsorbent: Kinetics and Equilibrium Modeling. *Journal of Bioremediation & Biodegradation*, *08*(03). https://doi.org/10.4172/2155-6199.1000395

FAO of United Nation. (2024). FAO Statistical Yearbook 2024 reveals critical insights on the sustainability of global agriculture, food security, and the importance of agrifood systems in employment. *2024 Statistical Yearbook*, 2024. https://www.fao.org/newsroom/detail/fao-statistical-yearbook-2024-reveals-critical-insights-on-the-sustainability-of-agriculture-food-security-and-the-importance-of-agrifood-in-employment/en

Foroutan, R., Peighambardoust, S. J., Mohammadi, R., Peighambardoust, S. H., & Ramavandi, B. (2022). Cadmium ion removal from aqueous media using banana peel biochar/Fe3O4/ZIF-67. *Environmental Research*, *211*, 113020. https://doi.org/10.1016/j.envres.2022.113020

Gupta, S. Sen, Al Kausor, M., & Chakrabortty, D. (2025). Banana peel as potential bioadsorbent toward removal of emerging contaminants from wastewater for sustainable environment: a review. *Chemical Papers*, *79*(5), 2717–2750. https://doi.org/10.1007/s11696-025-03945-5

Keerthana, B. G. T., Solaiyammal, T., Muniyappan, S., & Murugakoothan, P. (2018). Hydrothermal synthesis and characterization of TiO 2 nanostructures prepared using different solvents. *Materials Letters*, *220*, 20–23. https://doi.org/10.1016/j.matlet.2018.02.119

Lellala, K., Behera, S. K., Srivastava, P., Saeed, W. S., Haidyrah, A. S., & Burile, A. N. (2024). Fe3O4 nanoparticles decorated on N-doped graphene oxide nanosheets for elimination of heavy metals from industrial wastewater and desulfurization. *Diamond and Related Materials*, *150*, 111746. https://doi.org/10.1016/j.diamond.2024.111746

Liew, R. K., Nam, W. L., Chong, M. Y., Phang, X. Y., Su, M. H., Yek, P. N. Y., Ma, N. L., Cheng, C. K., Chong, C. T., & Lam, S. S. (2018). Oil palm waste: An abundant and promising feedstock for microwave pyrolysis conversion into good quality biochar with potential multi-applications. *Process Safety and Environmental Protection*, *115*, 57–69. https://doi.org/10.1016/j.psep.2017.10.005

Masoudi, R., Moghimi, H., Azin, E., & Taheri, R. A. (2018). Adsorption of cadmium from aqueous solutions by novel Fe3O4- newly isolated Actinomucor sp. bio-nanoadsorbent: functional group study. *Artificial Cells, Nanomedicine and Biotechnology*, *46*(sup3), S1092–S1101. https://doi.org/10.1080/21691401.2018.1533841

Mehmood, K., & Dhanya, W. M. (2025). Unlocking the potential of banana peel bioactives : extraction methods , benefits , and industrial applications. *Discover Food*. https://doi.org/10.1007/s44187-025-00276-y

Mishra, A., Kumari, M., Swati, Kumar, R., Iqbal, K., & Thakur, I. S. (2022). Persistent organic pollutants in the environment: Risk assessment, hazards, and mitigation strategies. *Bioresource Technology Reports*, *19*, 101143. https://doi.org/10.1016/j.biteb.2022.101143

Mishra, S., Prabhakar, B., Kharkar, P. S., & Pethe, A. M. (2023). *Banana Peel Waste : An Emerging Cellulosic Material to Extract Nanocrystalline Cellulose*. 8–13. https://doi.org/10.1021/acsomega.2c06571

Mor, S., & Ravindra, K. (2023). Municipal solid waste landfills in lower- and middle-income countries: Environmental impacts, challenges and sustainable management practices. *Process Safety and Environmental Protection*, *174*, 510–530. https://doi.org/10.1016/j.psep.2023.04.014

Otieno, A. O., Home, P. G., Raude, J. M., Murunga, S. I., Ngumba, E., Ojwang, D. O., & Tuhkanen, T. (2021). Pineapple peel biochar and lateritic soil as adsorbents for recovery of ammonium nitrogen from human urine. *Journal of Environmental Management*, *293*(February), 112794. https://doi.org/10.1016/j.jenvman.2021.112794

Pokharel, P., Kwak, J. H., Ok, Y. S., & Chang, S. X. (2018). Pine sawdust biochar reduces GHG emission by decreasing microbial and enzyme activities in forest and grassland soils in a laboratory experiment. *Science of the Total Environment*, *625*, 1247–1256. https://doi.org/10.1016/j.scitotenv.2017.12.343

Ramutshatsha-Makhwedzha, D., Mbaya, R., & Mavhungu, M. L. (2022). Application of Activated Carbon Banana Peel Coated with Al2O3-Chitosan for the Adsorptive Removal of Lead and Cadmium from Wastewater. *Materials*, *15*(3). https://doi.org/10.3390/ma15030860

Razzak, S. A., Faruque, M. O., Alsheikh, Z., Alsheikhmohamad, L., Alkuroud, D., Alfayez, A., Hossain, S. M. Z., & Hossain, M. M. (2022). A comprehensive review on conventional and biological-driven heavy metals removal from industrial wastewater. *Environmental Advances*, *7*(January), 100168. https://doi.org/10.1016/j.envadv.2022.100168

Selim, M. M., El-safty, S., & Tounsi, A. (2023). Review of the impact of the external magnetic field on the characteristics of magnetic nanofluids. *Alexandria Engineering Journal*, *76*, 75–89. https://doi.org/10.1016/j.aej.2023.06.018

Sial, T. A., Khan, M. N., Lan, Z., Kumbhar, F., Ying, Z., Zhang, J., Sun, D., & Li, X. (2019). Contrasting effects of banana peels waste and its biochar on greenhouse gas emissions and soil biochemical properties. *Process Safety and Environmental Protection*, *122*, 366–377. https://doi.org/10.1016/j.psep.2018.10.030

Smyth, S. (2024). *Waste Management in Developing Countries : Challenges and Solutions*. *09*. https://doi.org/10.37421/2475-7675.2024.9.350

Sossou, K., Bala Prasad, S., Agbotsou, K. E., Saidou Souley, H., & Mudigandla, R. (2024). Characteristics of landfill leachate and leachate treatment by biological and advanced coagulation process: Feasibility and effectiveness – An overview. *Waste Management Bulletin*, *2*(2), 181–198. https://doi.org/https://doi.org/10.1016/j.wmb.2024.04.009

Sossou, K., Prasad, S. B., Agbotsou, E. K., & Saidou Souley, H. (2024). Evaluation of the performance of magnetic zeolite nanocomposites in removing various water contaminants as heavy metals, organic pollutants, and emerging contaminants: A review. *Next Nanotechnology*, *6*(January), 100075. https://doi.org/10.1016/j.nxnano.2024.100075

Strategies, E. F., Ayach, J., Malti, W. El, Duma, L., Lalev, J., Ajami, M. Al, Hamad, H., & Hijazi, A. (2024). *Comparing Conventional and Advanced Approaches for Heavy Metal Removal in Wastewater Treatment : An In-Depth Review.*

Suttiponparnit, K., Jiang, J., Sahu, M., Suvachittanont, S., Charinpanitkul, T., & Biswas, P. (2011). Role of Surface Area, Primary Particle Size, and Crystal Phase on Titanium Dioxide Nanoparticle Dispersion Properties. *Nanoscale Research Letters*, *6*(1), 27. https://doi.org/10.1007/s11671-010-9772-1

Togun, H., Basem, A., Abdulrazzaq, T., Biswas, N., Abed, A. M., Dhabab, J. M., Mohammed, H. I., Sharma, B. K., Paul, D., & Barmavatu, P. (2025). Current developments in the use of nanotechnology to enhance the generation of sustainable bioenergy. *Sustainable Materials and Technologies*, *43*, e01266. https://doi.org/https://doi.org/10.1016/j.susmat.2025.e01266

Zanganeh, S., Kajbafvala, A., Zanganeh, N., Molaei, R., Bayati, M. R., Zargar, H. R., & Sadrnezhaad, S. K. (2011). Hydrothermal synthesis and characterization of TiO 2 nanostructures using LiOH as a solvent. *Advanced Powder Technology*, *22*(3), 336–339. https://doi.org/10.1016/j.apt.2010.04.010